



1 **Monsoon-facilitated characteristics and transport of atmospheric**
2 **mercury at a high-altitude background site in southwestern China**

3
4 Hui Zhang¹, Xuewu Fu^{1*}, Che-Jen Lin^{1,2}, Lihai Shang¹, Yiping Zhang³, Xinbin Feng^{1*}, Cynthia Lin⁴

5 ¹ State Key Laboratory of Environmental Geochemistry, Institute of Geochemistry, Chinese Academy of
6 Sciences, Guiyang 550002, PR China.

7 ² Center for Advances in Water and Air Quality, Lamar University, Beaumont, Texas 77710, United States.

8 ³ Xishuangbanna Tropical Botanical Garden, Chinese Academy of Sciences, Kunming 650223, China.

9 ⁴ The McKetta Department of Chemical Engineering, The University of Texas at Austin, Austin, Texas 78712,
10 United States.

11
12 Corresponding authors: Xinbin Feng (fengxinbin@vip.skleg.cn), Xuewu Fu (fuxuewu@mail.gyig.ac.cn)

13
14 **Abstract**

15 To better understand the influence of monsoonal climate and transport of atmospheric mercury (Hg) in
16 southwestern China, measurements of total gaseous mercury (TGM, defined as the sum of gaseous elemental
17 mercury, GEM, and gaseous oxidized mercury, GOM), particulate bound mercury (PBM) and GOM were carried
18 out at Ailaoshan Station (ALS, 2450 m a.s.l.) in southwestern China from May 2011 to May 2012. The mean
19 concentrations (\pm standard deviation) for TGM, GOM and PBM were 2.09 ± 0.63 ng m⁻³, 2.2 ± 2.3 pg m⁻³ and
20 31.3 ± 28.4 pg m⁻³, respectively. TGM showed a monsoonal distribution pattern with relatively higher
21 concentrations ($p=0.021$) during the Indian summer monsoon (ISM, from May to September) and the East Asia
22 summer monsoon (EASM, from May to September) periods than that in the non-ISM period. Similarly, GOM
23 and PBM concentrations were higher in the ISM period than in the non-ISM period. This study suggests that the
24 ISM and the EASM have a strong impact on long-range and transboundary transport of Hg between southwestern
25 China and South and Southeast Asia. Several high TGM events were accompanied by the occurrence of northern
26 wind during the ISM period, indicating anthropogenic Hg emissions from inland China could rapidly increase
27 TGM levels at ALS due to strengthening of the EASM. Most of the TGM and PBM events occurred at ALS
28 during the non-ISM period. Meanwhile, high CO concentrations were also observed at ALS, indicating that a
29 strong south tributary of westerlies could have transported Hg from South and Southeast Asia to southwestern
30 China during the non-ISM period. Consequently, southwestern China is an important anthropogenic source
31 region of ALS during the ISM period. The biomass burning in Southeast Asia and anthropogenic Hg emissions
32 from South Asia should be the source of atmospheric Hg in remote areas of southwestern China during the non-
33 ISM period.

34

35 **Keywords:** Atmospheric mercury, Indian summer monsoon, Transboundary transport, Southwestern China,
36 Southeast Asia



37 Introduction

38 Mercury (Hg), because of its volatility and long residence time in atmosphere, can transport a long distance with
39 air mass from anthropogenic Hg emission regions to remote areas (Schroeder and Munthe, 1998;Pirrone et al.,
40 2010). Therefore, the monsoonal climate can strongly affect the transport and distribution of atmospheric Hg in
41 monsoon regions, such as East and South Asia. The onset of ISM in May causes air masses, originating from the
42 Indian Ocean, to overpass South and Southeast Asia, and move northeastwardly to mainland China. Air
43 pollutants such as SO₂ and CO also travel into Mainland China via air transport caused by the ISM (Xu et al.,
44 2009;Bonasoni et al., 2010;Lin et al., 2013). In addition, the south tributary of westerlies, which passes over
45 northern India and Myanmar into southwestern China, can also carry air pollutants to southwestern China and
46 Tibetan plateau (Loewen et al., 2007;Xu et al., 2009;Yao et al., 2012). In East Asia, EASM is the dominant
47 monsoon. During the monsoon period (from May to September), the warm and moist air masses from the Pacific
48 Ocean sweep through the coastal area of China into inland China, and then move across southwestern China and
49 the eastern Tibetan plateau. During the non-ISM period (from October to April), the dry and cold air masses
50 from Siberia and Central Asia move through Mainland China into the Pacific Ocean via the westerlies (Hsu,
51 2005;Fan et al., 2013;Yu et al., 2015). The monsoonal wind changes play an important role in the transport of
52 regional Hg emissions in Southeast and East Asia (Sheu et al., 2010a;Tseng et al., 2012;Lee et al., 2016).

53

54 An increasing number of studies have indicated that pollutant emissions and transport originate from developing
55 countries in South and Southeast Asia (Wang et al., 2009;Lawrence and Lelieveld, 2010;Bonasoni et al.,
56 2010;Wang et al., 2015), home to more than a billion people with strong energy demands, can pose an impact to
57 other regions. These areas are regarded as important source regions of many air pollutants that pose significant
58 health risk locally and regionally (Rajgopal, 2003;Lelieveld et al., 2001). Previous studies indicated that Hg
59 emissions within South and Southeast Asia, including southwestern China, has significant impacts on the
60 distribution and deposition of atmospheric Hg in South and East Asia (Pirrone et al., 2009;Mukherjee et al.,
61 2009;Sheu et al., 2013;Fu et al., 2015;Zhang et al., 2012). These influences have raised concerns about/regarding
62 high atmospheric Hg levels in India and Southwestern China, and increased Hg contents in the snow packs of
63 Hindu Kush Himalayan-Tibetan glaciers (Loewen et al., 2005;Loewen et al., 2007;Kang et al., 2016). Previous
64 studies reported that the open biomass burning in forests and agricultural waste burning in Southeast Asia are
65 major sources for atmospheric Hg, aerosols and persistent organic pollutants in the region, which are subject to
66 trans-boundary transport (Reid et al., 2013;Chang et al., 2013;Zhang et al., 2010;Sheu et al., 2013;Zhang et al.,
67 2015;Wang et al., 2015). However, studies with respect to Hg emissions in South and Southeast Asia and the
68 associated transboundary transport mediated by monsoonal weather are still lacking.

69

70 In this study, we conducted comprehensive measurements of TGM, GOM and PBM at Ailaoshan Station (ALS),
71 a remote site in Southwestern China. ALS is located in the subtropical mountainous region of Yunnan province
72 and is close to South and Southeast Asia. The air flow to ALS is mainly controlled by the Indian monsoon



73 climate with plenty of rainfall (85% of the total annual rainfall occurred during the ISM period) and also can be
74 affected by EASM during the spring through early fall. In the winter, the weather is controlled by dry and cold
75 monsoon circulation including westerlies and the cold Siberian current (Liu et al., 2003b; Yuhong and Yourong,
76 1993; ZHAO et al., 2006). Therefore, ALS is as a unique location for studying the long-range and transboundary
77 transport of Hg influenced by the ISM and the EAMS.

78

79 In this paper, we present the observations of TGM, GOM and PBM during the ISM and non-ISM periods at ALS,
80 and discuss the transboundary transport characteristics using backward trajectory analysis. We also assess the
81 potential contributing sources of Hg, and analyze the pathways of transboundary transport. This study is part of
82 the Global Mercury Observation System (GMOS, <http://www.gmos.eu/>), which aims to establish a global
83 mercury monitoring network for ambient concentrations and deposition of Hg through ground-based
84 observational platforms and oceanographic aircraft campaigns (Sprovieri et al., 2013)

85

86 **2 Materials and methods**

87 **2.1 Measurement site descriptions**

88 This study was conducted at Ailaoshan Mountain National Natural Reserve (24°32'N, 101°01'E) which lies in
89 the Yunnan province of southern China, a protected forest section covering 5100 ha on the northern crest of a
90 pristine evergreen broad-leaved forest on Mt. Ailao (23°35'–24°44' N, 100°54'–101°01' E). The forest altitude
91 ranges from 2450 to 2650 m. above sea level (a.s.l.). The climate is influenced by both ISM and EASM during
92 warm seasons with plenty of rainfall. On the contrary, the dry and cold monsoon circulation from the south
93 tributary of westerlies control the climate of Mt. Ailao in the winter. Annual mean air temperature and rainfall
94 in the study area are 11.3 °C and 1947 mm, respectively (You et al., 2012). Mt. Ailao is regarded as the largest
95 tract (504 km²) of natural evergreen broad-leaved forest and one of China's most important natural areas which
96 has remained relatively undisturbed by human influences due to poor access (Liu et al., 2003a). Situated about
97 160 km to the south of Kunming, the capital of Yunnan province, ALS is relatively isolated from large
98 anthropogenic Hg sources. The nearest populated center is Jingdong County (Population: 36500, 1200 a.s.l.),
99 located 20 km to the south. Hg emissions in the Jingdong area is relatively low, ranging between 5-10 g km⁻²,
100 as displayed in Fig.1.

101

102 **2.2 Sampling methods and analysis**

103 **2.2.1 Measurements of atmospheric TGM, GOM and PBM**

104 From May 2011 to May 2012, TGM (GEM+GOM) in ambient air was measured every 5 minutes with an
105 automated mercury vapor analyzer, Tekran Model 2537A (Tekran Inc., Toronto, Canada), which is widely used
106 for monitoring atmospheric Hg. The automated instrument collects Hg on gold cartridges and then thermally
107 desorbs and detects the Hg by Cold Vapor Atomic Fluorescence Spectroscopy (CVAFS). The Tekran 2537A
108 performs automatic calibration for TGM every 73 hours using an internal permeation source. To evaluate these



109 automated calibrations, manual external injections using Tekran 2505 with known concentrations of Hg were
110 performed every 4 months. PBM ($\leq 0.2 \mu\text{m}$) were removed using a 47 mm diameter Teflon filter (pore size 0.2
111 μm). To prevent the effect of Hg emission from ground and GOM sorption, the A Teflon sampling line with its
112 inlet 5 m above the ground and heat preservation ($50 \text{ }^\circ\text{C}$) was employed at the sampling site. To mitigate the
113 influence of low atmospheric pressure on the pump's strain, a low sampling rate of 0.75 L min^{-1} (at standard
114 temperature and pressure)(Fu et al., 2008b;Swartzendruber et al., 2009;Zhang et al., 2015).

115

116 GOM and PBM was measured using a denuder-based system. The quartz denuders can collect GOM while air
117 passes through the KCl-coated surfaces. However, GOM and PBM have extremely low concentrations and
118 complex chemical reactivities in the atmosphere, and their chemical compounds are not well known. Several
119 previous studies reported that different GOM compounds (HgCl_2 , HgBr_2 and HgO) have different collection
120 efficiencies for the KCl-coated denuder surface, as high relative humidity can passivate KCl-coated denuder and
121 make GOM recoveries decrease (Huang et al., 2013a;Gustin et al., 2015;Huang and Gustin, 2015). In this study,
122 the measurements of GOM and PBM were achieved by a manual method. The procedure of sampling and
123 analysis of the manual method is analogous to the Tekran speciation system using identical denuders to the
124 Tekran system with KCl coating (Gustin et al., 2015), differing only by manual operation. Details regarding
125 the measurement system and the quality assurance routines are presented in earlier works (Xiao et al.,
126 1997;Landis et al., 2002;Feng et al., 2000;Fu et al., 2012c;Zhang et al., 2015).

127

128 Four sampling campaigns were carried out for PBM and GOM measurements: August 17–24, 2011, December
129 3–17, 2011, April 12–19, 2012, and July 11–21, 2012. The selected periods represented the ISM period (May
130 and September) and non-ISM period (October and April) observations. Before sampling, the denuders were pre-
131 cleaned by pyrolysis to obtain the filed blanks, which was at $1.2 \pm 0.7 \text{ pg}$ ($N=12$) for denuders. The quartz fiber
132 filter was heated at $900 \text{ }^\circ\text{C}$ for 30 minutes for pre-cleaning. A somewhat higher field blank ($6.2 \pm 2.7 \text{ pg}$, $N=20$)
133 was observed and used to correct the PBM concentrations by subtracting the mean blank from the detected Hg.
134 In this study, data QA procedure followed the GMOS Standard Operation Procedure and Data Quality
135 Management (D'Amore et al., 2015).

136

137 **2.2 Meteorological data and backward trajectory calculation**

138 Meteorological parameters, including rainfall (RF), wind direction (WD), wind speed (WS), air temperature (AT)
139 and relative humidity (RH), were provided by the local weather station from ALS. In order to identify the
140 influence of long-range transport on the measured Hg at the study site, three-day backward trajectories were
141 calculated using HYSPLIT and the Global Data Assimilation System (GDAS) meteorological data archives of
142 the Air Resource Laboratory, National Oceanic and Atmospheric Administration (NOAA). The meteorological
143 data are of $1^\circ \times 1^\circ$ spatial resolutions at 6-hour intervals. All the backward trajectories ended at the sampling site



144 at an arrival height of 500 m above the ground. The backward trajectories were calculated at 1-hour intervals,
145 and cluster analysis of the trajectory endpoints was performed to determine the regional transport pathway. To
146 distinguish the larger sources from moderate sources, a weighing algorithm based on measured concentrations
147 (concentration weighted trajectory (CWT)) was applied in this study. In this procedure, each grid cell received
148 a source strength obtained by averaging sample concentrations that have associated trajectories that crossed that
149 grid cell as follows:

$$150 \quad C_{ij} = \frac{1}{\sum_{l=1}^M \tau_{ijl}} \sum_{l=1}^M C_l \tau_{ijl}$$

151 C_{ij} is the average weighted concentration in the grid cell (i,j) . C_l is the measured Hg concentration, τ_{ijl} is the
152 number of trajectory endpoints in the grid cell (i,j) associated with the C_l sample, and M is the number of samples
153 that have trajectory endpoints in grid cell (i,j) . A point filter is applied as the final step of CWT to eliminate grid
154 cells with few endpoints. Weighted concentration fields show concentration gradients across potential sources.
155 This method helps determine the relative significance of potential sources (Hsu et al., 2003; Cheng et al., 2013).

156

157 **3 Results and discussion**

158 **3.1. Features of monsoonal transport and characteristics observed Hg species**

159 **3.1.1 General distribution characteristics of TGM in atmosphere**

160 The highly time-resolved long-term data set of TGM concentrations in ambient air at ALS is displayed in Fig.
161 2, and the mean TGM concentration over the sampling period was $2.09 \pm 0.63 \text{ ng m}^{-3}$ with a higher level (2.22 ng
162 m^{-3}) during the ISM period than that during the non-ISM period (1.99 ng m^{-3}) (Table 1). The TGM mean
163 concentration at ALS was slightly higher than that of the global background ($1.5\text{-}1.7 \text{ ng m}^{-3}$ in the Northern
164 Hemisphere and $1.1\text{-}1.3 \text{ ng m}^{-3}$ in the Southern Hemisphere (Lindberg et al., 2007; Slemr et al., 2015; Venter et
165 al., 2015), and higher than those (1.58 to 1.93 ng m^{-3}) observed in some remote areas in northern America and
166 Europe (Kim et al., 2005; Sprovieri et al., 2010). Compared to the background concentrations observed at the
167 Shangri-La Baseline Observatory in Yunnan province ($2.55 \pm 0.73 \text{ ng m}^{-3}$, (Zhang et al., 2015), at Mt. Leigong in
168 Guizhou province ($2.80 \pm 1.51 \text{ ng m}^{-3}$, (Fu et al., 2010b) and at Mt. Gongga in Sichuan province $3.98 \pm 1.62 \text{ ng}$
169 m^{-3} , (Fu et al., 2008a), the mean TGM level at ALS was lower. However, the mean TGM level at ALS was higher
170 than those observed at Mt. Changbai ($1.60 \pm 0.51 \text{ ng m}^{-3}$) in Northeast China and at Mt. Waliguan (WLG)
171 Baseline Observatory ($1.98 \pm 0.98 \text{ ng m}^{-3}$) in the Tibetan plateau (Fu et al., 2012a; Fu et al., 2012b). Interestingly,
172 most peaks of high TGM concentrations at ALS frequently appeared during the ISM period (Fig. 2). This differed
173 from the previous results at Mt. Gongga and Mt. Leigong of southwestern China but was similar to the results
174 at Shangri-La. There were also several peaks that appeared during the non-ISM period, which could have been
175 caused by different sources than those during the ISM period. The sampling site is located adjacently to South
176 Asia and Southeast Asia, and Hg emissions from biomass burning in South Asia and Southeast Asia would
177 inevitably contribute to the elevated TGM concentrations at ALS during the non-ISM period (Wang et al., 2015).
178 Southwestern China is one of the largest Hg emission areas in China, and coal combustion and non-ferrous metal



179 (especially zinc) smelting activities are the two main Hg sources. It was reported that total Hg emission from
180 Guizhou, Sichuan and Yunan provinces reached about 128 tons in 2003 (Wu et al., 2006), and the large amount
181 of Hg emissions contributed to the elevation of TGM concentrations in this area. Since Guizhou, Sichuan and
182 Yunan provinces are located in the upper wind direction of the sampling site to EASM, Hg emission from these
183 areas can be transported to ALS and result in the elevation of TGM concentrations.

184

185 **3.1.2 Monthly TGM anomalies and wind meteorology**

186 To assess the monsoonal variation of TGM concentrations, the distribution of monthly mean TGM
187 concentrations at ALS is shown in Fig. 3. The Hg concentrations during the ISM period were higher than those
188 during the non-ISM period. The highest monthly concentration was observed in May with a mean value of 2.46
189 ng m^{-3} , and the lowest monthly mean concentration of 1.45 ng m^{-3} was observed in November. Although there
190 were relatively higher Hg levels in December and January during the non-ISM period, this pattern was generally
191 different from the most common pattern in the Northern Hemispheric which has a summer minimum and winter
192 maximum TGM distribution pattern as observed in many previous studies (Kellerhals et al., 2003; Kock et al.,
193 2005; Fu et al., 2010a). There were several possible reasons for this monsoonal distribution pattern of TGM
194 concentrations on ALS.

195

196 Firstly, the increase of TGM concentrations during the ISM period could be due to the interaction of the EASM
197 and the ISM, promoting the air masses with high Hg from the areas of anthropogenic Hg emissions to ALS.
198 Generally, ALS is located on the low latitude highlands of Yunnan in southwestern China which is subject to
199 the interactions between the EASM and the ISM, although most of time, the air flow of Yunnan is mainly
200 controlled by the ISM during the ISM period. However the strengthening of the EASM or the weakening of the
201 ISM can also spur the EASM to control this area and bring precipitation during the ISM period (Fan et al., 2013).
202 Therefore, the TGM level should be sensitive to the strengthening/weakening of the two monsoons. Once the air
203 flow from high Hg source regions (Sichuan, Guizhou and Chongqing) is transported to ALS with the
204 strengthening of the EASM, TGM levels at ALS can increase rapidly. However, anthropogenic Hg emissions
205 from inland China could increase the Hg background level with the raid of westerlies and cold Siberian current
206 during the non-ISM period. Previous studies discussed the seasonal change of TGM at the background sites of
207 southwestern China and found that increased domestic coal consumption and an increase in household heating
208 was the main cause of elevated TGM concentrations observed in winter (Fu et al., 2008a; Fu et al., 2010a).
209 Additionally, the biomass burning in Southeast Asia could also be an important reason for high Hg level at ALS
210 during the non-ISM period. Intense biomass burning originating from Southeast Asia typically occurred in late
211 winter and spring (Huang et al., 2013b). This could be the cause of the high TGM at ALS along with the long-
212 range transboundary transport in the spring (Wang et al., 2015).

213

214 Fig. 4 displays the distribution frequency of TGM above and under the average (2.09 ng m^{-3}) based on wind



215 direction including Northeast (NE), Southeast (SE), Southwest (SW) during the ISM and non-ISM period. It is
216 clear that SW was the predominating wind direction, and there was no Northwest (NW) during the entire study
217 period. The SW frequency was highest when high and low Hg levels occurred during the ISM period or non-
218 ISM period, and the SW frequency showing low Hg was higher than that of high Hg. This could be the reason
219 why the average Hg level from SW was not high. The air flows originating from South Asia and Southeast Asia
220 could contribute to high Hg concentrations at ALS. Contrarily, NE and SE frequency had a relatively lower trend
221 than SW, but high Hg frequency from NE and SE were both high during the ISM period. This should be the
222 result from the strengthening of EASM during the ISM period. However, during the non-ISM period, the cold
223 and dry air flow from the south tributary of westerlies could have swept over South Asia and Southeast Asia and
224 moved to ALS with high wind speed (Fig. 3). This dry air flow could have also taken the air masses of high Hg
225 levels emitted from biomass burning in South Asia and Southeast Asia to ALS and caused a rapid increase of
226 Hg level at ALS. In addition, cold air flows could also transport Hg emitted from inland China to ALS due to
227 the strengthening of the cold Siberian current during the non-ISM period. Therefore, there were some high TGM
228 events in December and March at ALS (Fig. 3).

229

230 **3.1.3 Seasonal variation of GOM and PBM influenced by monsoonal weather**

231 Table 1 shows seasonal statistics of daily averages for Hg species and select meteorological parameters which
232 were determined on a seasonal basis and for the year-long dataset. TGM during the ISM period was statistically
233 higher than during the non-ISM period (Table S1). Meanwhile, AT, RF and RH had a monsoonal distribution
234 with the highest level during the ISM period, and SW frequency had decline with increase of SE and NE
235 frequency during the ISM period. This suggests the EASM could also influence the climate at ALS during the
236 ISM period, which was consistent with TGM concentration that the site is impacted by regional sources including
237 biomass burning and monsoonal long-range transboundary transport.

238

239 For GOM and PBM, which on average accounted for <2% of the TGM, there were also seasonal trends. Both
240 species had the highest levels in autumn while GOM was lowest in the winter and PBM was lowest in the spring.
241 The lowest GOM level was observed in the summer, which increased consistently to reach the highest value
242 (3.4 ± 3 pg m⁻³) in autumn. Similarly, PBM displayed the same distribution in seasonal variation, with the highest
243 PBM level in autumn (46.3 ± 28.8 pg m⁻³). Meanwhile, the AT, RF and RH were also higher during the ISM
244 period than those during the non-ISM period. However, unlike TGM, the GOM and PBM were closely linked
245 with atmospheric Hg chemistry, meteorological patterns, and numerous other factors. Thus, there are several
246 likely factors that contribute to these trends, including a greater number of sources during the ISM period, and
247 changing ecological or meteorological conditions. Previous studies in the Mt. Gongga and Mt. Leigong area
248 suggested that enhanced coal and biomass burning played a significant role in elevated TGM concentrations
249 during cold seasons (Fu et al., 2008a; Fu et al., 2010a). Enhanced coal and biomass burning during cold seasons
250 is generally driven by the need for residential heating in China. However, in the southern Yunnan province, the



251 air temperature is high during the non-ISM period. Thus, the domestic use of coal is not dominant for residential
252 heating, but rather the agricultural activity in the region including the crop harvesting and the burning of straw.
253 This was probably one of most important reasons for the highly elevated GOM and PBM level at ALS in autumn.
254

255 Monsoonal distribution patterns and mean TGM, GOM and PBM concentrations based on the four sampling
256 campaigns in ALS are shown in Fig. 5. Mean concentration of the three Hg species showed a monsoonal
257 variation with higher levels during the ISM period than during the non-ISM period. This suggests that regional
258 anthropogenic emissions are important Hg sources in southwestern China. During the ISM period, not only was
259 air flow originating from the Indian Ocean dominating, but air flow that occasionally originated from the Pacific
260 Ocean also intruded the study site, which passed through central and southwestern China, one of the most Hg-
261 polluted regions. Moreover, the TGM, GOM and PBM levels from the north wind were higher than those from
262 the south wind to ALS (Fig. S1). Thus, the air masses likely captured large amounts of Hg during transport and
263 caused elevated atmospheric Hg concentrations at ALS during the ISM period.

264

265 Fig. 6 shows pollution roses of TGM, GOM and PBM at ALS during the ISM period and during the non-ISM
266 period respectively. The wind direction at the study site was dominantly SW. This reflects that the predominant
267 monsoon influence the ALS site is the ISM and westerlies. During the ISM period, most of the TGM, GOM and
268 PBM events were from SW, slightly fewer were from NE, and both SW and NE exhibited higher TGM, GOM
269 and PBM events. This indicates SW and NE were the two primary directions of high Hg sources during the ISM
270 period. However, during the non-ISM period, almost all TGM, GOM and PBM events were from SW. This
271 indicates that strong westerlies were the primary winds during the non-ISM period. These westerlies could take
272 the Hg from South Asia and Southeast Asia into southwestern China. Thus, the dependence of atmospheric Hg
273 species on wind was likely attributed to an interplay of regional sources and the long-range transboundary
274 transport of Hg.

275

276 Indeed, GOM concentrations were extremely low at ALS. Marine air masses during the ISM period likely diluted
277 the atmospheric Hg in the study area. The high RF and low WS can promote the wet deposition of GOM and
278 PBM. Therefore, in the summer, RH was very high, but the GOM and PBM were very low at ALS. A new study
279 reported that high RH could reduce the collection of GOM by the KCl-coated denuder (Huang, Gustin et al.
280 2015). This could be another reason why the GOM was low in summer. Additionally, low GOM and PBM could
281 be also related to rapid deposition of Hg due to the high altitude montane environment and luxuriant virgin forest
282 cover of Mt. Ailao. A previous study already found that the increasing occurrence and extension of fog and cloud
283 droplet interception can enhance the uptake of Hg by foliage (Zhang et al., 2013). We will study the possible
284 reasons why the GOM level is exceedingly low in ALS via continuous long-term monitoring for GOM in the
285 future.

286



287 3.2 Transboundary transport of Hg facilitated by monsoons

288 The backward trajectories arriving at ALS over the study period were grouped into five clusters, which are shown
289 in Fig. 7. Most of these backward trajectories consisted of air masses that originated from the South Asia and
290 Southeast Asia, passing over India, Bengal Bay, the Indo-China peninsula and the southern Yunnan province of
291 China. Just 4.7% of air masses originated from inland China and then passed over Sichuan, Guizhou, Yunnan
292 provinces and the city of Chongqing, China. For the five types of air masses, air masses in cluster 1 displayed
293 very low TGM concentrations (1.86 ng m^{-3}) for all the air masses, although their frequencies were the highest
294 (38.55%). Similarly, the mean TGM concentration in cluster 3 was 1.92 ng m^{-3} , which was also considerably
295 low and had second highest frequency (23.03%). This suggest that Hg emitted in South Asia could not have
296 largely contributed to the high Hg levels at ALS. Air masses in cluster 4 showed a high TGM concentration of
297 2.42 ng m^{-3} , which originated over the South China Sea and passed over northern Vietnam and Laos and the
298 southern Yunnan and Guangxi provinces of China, which are generally areas of less anthropogenic emissions
299 other than biomass burning during the non-ISM period. However, the air masses in cluster 5 were also polluted
300 with Hg, with a mean concentration of 2.20 ng m^{-3} , which is higher than those of clusters 1, 3 and 4. Air flows
301 likely originated in Bengal Bay and passed over Myanmar since most anthropogenic emissions in Myanmar are
302 centralized in southern Myanmar, and intense biomass burning in the area during the non-ISM period perhaps
303 contributed to a slightly high TGM level of these air masses. Cluster 2 displayed the highest TGM concentrations
304 (2.65 ng m^{-3}). Air masses in cluster 2 passed over the inland China region, which is the most densely populated
305 and heavily Hg-polluted area in China due to industrial and domestic coal combustion, smelting industries,
306 cement production, biomass burning, etc. Sichuan, Guizhou, Chongqing and the northwestern Yunnan provinces,
307 respectively, were contributing Hg source provinces in China. Although only 4.70% of air masses were from the
308 southwestern China region, the TGM concentrations of these air masses were the highest, which could be an
309 important reason for elevated TGM levels at ALS.

310

311 The Tibetan plateau and Yunnan-Guizhou plateau are located in north of ALS, which is a monitoring site at
312 high elevation. To the south of ALS, the geography consists of a montane area plain of low elevation. Thus, the
313 air masses at ALS were from different directions and of different heights, which may have affected the Hg level
314 in the air masses as they passed over different anthropogenic emission regions. Fig. S2 compares the three-
315 dimensional height of all the wind clusters arriving at ALS. The height of cluster 1 from India was the highest.
316 Such transport pattern tends to more effectively dilute Hg emissions from low altitude surface to ALS. Thus, in
317 non-ISM period, the south tributary of westerlies passed over India does not lead to elevated Hg concentrations
318 at ALS. Additionally, due to the high Hg concentration in the air in southwestern China, the TGM level of any
319 air masses coming from the northeast of ALS should be increased at ALS regardless of height. Contrarily, cluster
320 3 had a high height but low level TGM because its air masses originated and passed over the area of low
321 anthropogenic emission region.

322



323 3.3 Impacts of Hg emission from industrial sources and biomass burning

324 Fig. 8 shows the seasonal trend analysis using the average of the daily TGM values, RF distribution, WS and
325 WD during the study period along with IMI (Indian monsoon index) at ALS. In general, May to September
326 represent the normal ISM period. The IMI, however, also illustrates the onset in of the ISM in May and its retreat
327 at the end of September. During the ISM period, the mean TGM is 2.22 ng m^{-3} , which is slightly higher than
328 1.99 ng m^{-3} during the non-ISM period, and most of the RF events appeared during the ISM period. More
329 crucially, some high-frequency NE and east wind events occurred during the ISM period. Once the WD shifted
330 from SW to NE, the TGM level rapidly increased in addition to relatively lower RF and WS. This indicates that
331 the strengthening of EASM can move the air masses with high Hg levels from inland China to ALS, but when
332 the NE air flow climbed over the Yunnan-Guizhou plateau, the speed of air mass movement decreased and
333 carried less RF. However, during the non-ISM period, the high TGM events did not accompany the appearance
334 of NE. The WD was primarily SW other than a few SE at the end of March, and the WS was higher than the
335 level during the ISM period. This indicates that the south tributary of westerlies could control the climate and
336 carry air masses from South Asia and Southeast Asia. High Hg events were also evident with SW and SE during
337 the non-ISM period, which could be due to Hg emission from biomass burning in South Asia and Southeast Asia.

338
339 Therefore, five special high TGM events were accompanied by an exceeding variation of WD and WS to analyze
340 the reasons of high TGM appearance. As Fig. 8 shows, five extreme peaks of high TGM were displayed from
341 June 23-29 and July 10-18, 2011, September 28 to October 9 and December 23-31, 2011, and March 23-29,
342 2012, respectively. On June 23, the air masses from India began to increase TGM concentrations, and with the
343 strengthening of the EASM, the TGM level increased gradually and peaked with low RF and WS on June 26.
344 Meanwhile, the air masses that had just swept Chongqing, Sichuan, Guizhou and eastern Yunnan provinces,
345 including Kunming city, where there is high Hg emission because of industrial activities (Fig. 1). Thus the air
346 flow from these areas could suddenly increase the TGM level at ALS due to the long-range transport. Once the
347 air flow from EASM faded away, the ISM would control the ALS area again, the air flow would shift to
348 southwest, and the TGM level would return to average levels (Fig. 9a). The same variation appeared from July
349 10-18 during the ISM period. TGM levels increased on July 10 and were highest (3.65 ng m^{-3}) from July 14-16
350 with the strengthening of EASM. When WD shifted to SW, TGM was back to its base level (Fig. 9b). In fact,
351 during the ISM period, this sort of peak appeared many times (Fig. 2), the reason for these peaks being similar
352 to the two peaks in June and July.

353
354 However, on September 28, due to the fadeaway of ISM and the strengthening and incursion of air flow from
355 EASM as well as the cold Siberian current, a high TGM event was initiated as the air flow shifted from SW to
356 NE (Fig. 10). When the air flow swept Chongqing, Sichuan, Guizhou and eastern Yunnan province again from
357 September 30 to October 5, the TGM level increased to its highest level (3.18 ng m^{-3}), then gradually decreased
358 with the shift in air flow that swept northern Vietnam and Laos. These high Hg events happened during the



359 transitional period from the ISM period to the non-ISM period, which indicates that the high Hg emission from
360 inland China had severely influenced the TGM level at ALS. As previously discussed, the strengthening of the
361 EASM or the weakening of ISM caused the air flow with high Hg originating from inland China to be transported
362 to ALS, which contributed to extremely high TGM concentrations.

363

364 During the non-ISM period, with the fading of the ISM and EASM, the south tributary of westerlies grew
365 stronger as the dry and cold air flow swept over South and Southeast Asia and arrived in southwestern China to
366 control the climate. Hence, industrial sources likely contributed to the high level Hg concentrations in this study
367 site. In Fig. 11, when air masses entered from important Southeast Asia industrial regions (e.g. Hanoi, Haiphong
368 et al.), the TGM level was highest (3.13 ng m^{-3}) while TGM concentrations decreased 11% with the entrance of
369 the strong wind from the Bay of Bengal. In addition, fire events were also observed along the backward
370 trajectories. Moreover, the high correlation ($R^2=0.89$) between Hg and CO was identified in Fig. 12. However,
371 the TGM/CO ratio was $0.01124 \text{ ng g}^{-1} \text{ ppb}^{-1}$ ($1.80 \text{ E-6 mol mol}^{-1}$), which is more than 10 times higher than the
372 reported world average biomass burning ratio but was close to ratios observed in Taiwan in October (1.28 E-6 ,
373 verified from anthropogenic plumes) Sheu et al. (2010b);(Friedli et al., 2009). Therefore, in this event, the major
374 contributor should be the industrial sources from Southeast Asia. Fig. 13 shows that biomass burning is an
375 important source for Hg. On March 23, the high TGM concentrations began to arise because of the fire events
376 that occurred in northeastern India and north Myanmar. TGM levels were highest (4.53 ng m^{-3}) when the air
377 flow shifted and swept inland China. When the air flow shifted from east to southwest and swept south Myanmar
378 from March 25-28, a period of were high-frequency fire events, the TGM concentrations maintained a high level
379 (3.11 ng m^{-3}). However, when the air flow shifted to northern Myanmar, the TGM level returned to low levels
380 (2.01 ng m^{-3}), indicating that biomass burning originating from Southeast Asia could also rapidly input and
381 increase the TGM levels in southwestern China during the non-ISM period. Different from Fig. 12, the TGM/CO
382 ratio decreased by half in Fig. 14 and was comparable with reported biomass burning ratios (3.00 E-7) in Canada
383 and the USA (Sigler et al., 2003). Moreover, the close correlations between TFRP (total fire radiative power),
384 which provides information on the measured radiant heat output of detected fires, and CO ($R^2=0.98$) and TGM
385 ($R^2=0.45$) verify the above hypothesis (Wooster et al., 2005).

386

387 **3.4 Potential source regions of atmospheric Hg**

388 Fig. 15a shows the possible source regions and pathways of atmospheric Hg at ALS during the ISM period
389 identified by the CWT analysis. Sichuan, Guizhou, Chongqing, Yunnan and Guangxi provinces in southwestern
390 China as well as in Southeast Asia as well as northern Laos, Cambodia, Thailand and Vietnam were likely source
391 regions of high atmospheric Hg at ALS during the ISM period. Southwestern China, including Sichuan,
392 Chongqing, Guizhou, and Yunnan provinces, is an important anthropogenic source region of China (Wang et al.,
393 2006;Feng and Qiu, 2008;Wu et al., 2006;Jiang et al., 2006). In fact, several capital cities including Kunming,
394 Guiyang and Chongqing are located about 200 to 800 km north of ALS. These capital cities may be the source



395 of much of the Hg emissions during atmospheric transport. The identified source areas correspond very well
396 with the anthropogenic Hg emission inventories in East and South Asia. The potential area identified in Southeast
397 Asia is also classified as a high anthropogenic Hg emission region by Hg emission inventories (Pacyna et al.,
398 2010;Pirrone et al., 2010;Li et al., 2009), and the biomass burning in Southeast Asia could cause high Hg
399 emissions. During the non-ISM period, as displayed in Fig. 15b, Northern India is an important urbanized and
400 industrialized area that may produce high anthropogenic Hg emission rates, as there are a number of large scale
401 industries and coal-fired power plants in India (Burger Chakraborty et al., 2013;Pervez et al., 2010). Additionally,
402 the biomass burning in Southeast Asia should be a large contributor of high TGM levels at ALS (Wang et al.,
403 2015). A small region in eastern Myanmar and northern Laos and Thailand was also identified as a potential
404 source region and pathway for TGM at ALS. The high CWT values in this area may be primarily due to high
405 Hg emission rates because of biomass burning during the non-ISM period.

406

407 Indeed, the emission of Hg from biomass burning includes forest fire and agricultural waste burning in Southeast
408 Asia and southwestern China and could also play an important role in TGM distribution and transboundary
409 transport at ALS. Southeast Asia and southwestern China are large tropical rain forest areas. During the ISM
410 period, the air had a very high RH and the highest RF. Because the fire events in Southeast Asia and southwestern
411 China were not frequent and the biomass burning for agriculture was not prevalent, less Hg from biomass burning
412 was released into the atmosphere. As shown in Fig. S3a, fire events in Southeast Asia and southwestern China
413 during the ISM period (mainly from June to September 2011) exhibited a much lower frequency, indicating that
414 the significant impact of Hg transport was primarily from anthropogenic Hg emissions. Nevertheless, during the
415 non-ISM period (mainly from December 2011 to April 2012), high-frequency fire events in Southeast Asia and
416 southwestern China were observed (Fig. S3b). Hg emissions from fire events peaked when the most intense
417 biomass burning occurred in Southeast Asia and Southwest China. This increased TGM level at ALS once air
418 masses from these areas were transported to ALS.

419

420 **4 Conclusions**

421 This study made at ALS suggests a significant impact of monsoonal climates on the distribution and long-range
422 transport of atmospheric Hg in southwestern China and shows a pronounced monsoonal variation with a high
423 TGM level during the ISM period and a low TGM level during the non-ISM period. This seasonal variation
424 opposes the previous distribution of atmospheric Hg observed in the background sites of southwestern China.
425 This behavior seems to be dominated by the seasonal variation of monsoons and the influence of the long-range
426 and transboundary transport of Hg from high anthropogenic Hg emissions and biomass burning. The high Hg
427 regional sources from inland China were an important factor in the elevated TGM level. Meanwhile, with the
428 economy developing rapidly, anthropogenic Hg emission in Southeast Asia is also increasing. This will elevate
429 the TGM level in the area, including that of southwestern China. Additionally, Hg emitted from India can travel
430 to southwestern China due to the ISM in the summer and a strong south tributary of westerlies during cold



431 seasons. Biomass burning includes high-frequency fire events in Southeast Asia that could play an important
432 role for high TGM levels during the non-ISM period. Thus, the TGM concentrations during different seasons in
433 addition to the impacts of monsoonal climate may pose an important constraint on the global models of
434 atmospheric Hg.

435

436 **Acknowledgments.** This work is supported by the National “973” Program of China (2013CB430003), the
437 National Science Foundation of China (41430754, 41473025, 41273145, 41173024). We also thank Xin Luo,
438 Ben Yu and Jun Zhou for field sampling assistance.

439

440 **Reference**

441 AMAP/UNEP: Technical Background Report for the Global Mercury Assessment 2013, in: Arctic Monitoring and
442 Assessment Programme, Oslo, Norway/UNEP Chemicals Branch Geneva, Switzerland, 2013.

443 Bonasoni, P., Laj, P., Marinoni, A., Sprenger, M., Angelini, F., Arduini, J., Bonafe, U., Calzolari, F., Colombo, T., and
444 Decesari, S.: Atmospheric Brown Clouds in the Himalayas: first two years of continuous observations at the Nepal-
445 Climate Observatory at Pyramid (5079 m), Atmospheric Chemistry and Physics Discussions, 10, 4823-4885, 2010,
446 doi:10.5194/acp-10-7515-2010.

447 Burger Chakraborty, L., Qureshi, A., Vadenbo, C., and Hellweg, S.: Anthropogenic mercury flows in India and impacts
448 of emission controls, Environmental science & technology, 47, 8105-8113, 2013, doi: 10.1021/es401006k.

449 Chang, S.-S., Lee, W.-J., Wang, L.-C., Lin, N.-H., and Chang-Chien, G.-P.: Influence of the Southeast Asian biomass
450 burnings on the atmospheric persistent organic pollutants observed at near sources and receptor site, Atmospheric
451 Environment, 78, 184-194, 2013, doi:10.1016/j.atmosenv.2012.07.074.

452 Cheng, I., Zhang, L., Blanchard, P., Dalziel, J., and Tordon, R.: Concentration-weighted trajectory approach to
453 identifying potential sources of speciated atmospheric mercury at an urban coastal site in Nova Scotia, Canada, Atmos
454 Chem Phys, 13, 6031-6048, 10.5194/acp-13-6031-2013, 2013, doi:10.5194/acp-13-6031-2013.

455 D'Amore, F., Bencardino, M., Cinnirella, S., Sprovieri, F., and Pirrone, N.: Data quality through a web-based QA/QC
456 system: implementation for atmospheric mercury data from the global mercury observation system, Environ Sci-Proc
457 Imp, 17, 1482-1491, 10.1039/c5em00205b, 2015, doi: 10.1039/C5EM00205B.

458 Fan, H., Hu, J., and He, D.: Trends in precipitation over the low latitude highlands of Yunnan, China, Journal of
459 Geographical Sciences, 23, 1107-1122, 2013, doi: 10.1007/s11442-013-1066-y.

460 Feng, X., Sommar, J., Gårdfeldt, K., and Lindqvist, O.: Improved determination of gaseous divalent mercury in
461 ambient air using KCl coated denuders, Fresenius' journal of analytical chemistry, 366, 423-428, 2000, doi:
462 10.1007/s002160050086.

463 Feng, X., and Qiu, G.: Mercury pollution in Guizhou, Southwestern China—an overview, Science of the Total
464 Environment, 400, 227-237, 2008, doi:10.1016/j.scitotenv.2008.05.040.

465 Friedli, H. R., Arellano, A. F., Cinnirella, S., and Pirrone, N.: Initial Estimates of Mercury Emissions to the
466 Atmosphere from Global Biomass Burning, Environ Sci Technol, 43, 3507-3513, 2009, doi: 10.1021/es802703g.

467 Fu, X., Feng, X., Zhu, W., Wang, S., and Lu, J.: Total gaseous mercury concentrations in ambient air in the eastern



- 468 slope of Mt. Gongga, South-Eastern fringe of the Tibetan plateau, China, *Atmospheric Environment*, 42, 970-979,
469 2008a, doi:10.1016/j.atmosenv.2007.10.018.
- 470 Fu, X., Feng, X., Dong, Z., Yin, R., Wang, J., Yang, Z., and Zhang, H.: Atmospheric gaseous elemental mercury (GEM)
471 concentrations and mercury depositions at a high-altitude mountain peak in south China, *Atmospheric Chemistry and*
472 *Physics*, 10, 2425-2437, 2010a, doi:10.5194/acp-10-2425-2010.
- 473 Fu, X., Feng, X., Liang, P., Zhang, H., Ji, J., and Liu, P.: Temporal trend and sources of speciated atmospheric mercury
474 at Waliguan GAW station, Northwestern China, *Atmospheric Chemistry and Physics*, 12, 1951-1964, 2012a,
475 doi:10.5194/acp-12-1951-2012.
- 476 Fu, X., Feng, X., Shang, L., Wang, S., and Zhang, H.: Two years of measurements of atmospheric total gaseous
477 mercury (TGM) at a remote site in Mt. Changbai area, Northeastern China, *Atmospheric Chemistry and Physics*, 12,
478 4215-4226, 2012b, doi:10.5194/acp-12-4215-2012.
- 479 Fu, X. W., Zhang, H., Lin, C. J., Feng, X. B., Zhou, L. X., and Fang, S. X.: Correlation slopes of GEM/CO, GEM/CO₂,
480 and GEM/CH₄ and estimated mercury emissions in China, South Asia, the Indochinese Peninsula, and Central Asia
481 derived from observations in northwestern and southwestern China, *Atmos Chem Phys*, 15, 1013-1028, 2015,
482 doi:10.5194/acp-15-1013-2015.
- 483 Gustin, M. S., Amos, H. M., Huang, J., Miller, M. B., and Heidecorn, K.: Measuring and modeling mercury in the
484 atmosphere: a critical review, *Atmos Chem Phys*, 15, 5697-5713, 10.5194/acp-15-5697-2015, 2015, doi:10.5194/acp-
485 15-5697-2015.
- 486 Hsu, H.-H.: East asian monsoon, in: *Intraseasonal Variability in the atmosphere-ocean climate system*, Springer, 63-
487 94, 2005, doi: 10.1007/3-540-27250-X_3.
- 488 Hsu, Y.-K., Holsen, T. M., and Hopke, P. K.: Comparison of hybrid receptor models to locate PCB sources in Chicago,
489 *Atmospheric Environment*, 37, 545-562, 2003, doi:10.1016/S1352-2310(02)00886-5.
- 490 Huang, J., Miller, M. B., Weiss-Penzias, P., and Gustin, M. S.: Comparison of gaseous oxidized Hg measured by KCl-
491 coated denuders, and nylon and cation exchange membranes, *Environ Sci Technol*, 47, 7307-7316, 2013a,
492 doi: 10.1021/es4012349
- 493 Huang, J. Y., and Gustin, M. S.: Uncertainties of Gaseous Oxidized Mercury Measurements Using KCl-Coated
494 Denuders, Cation-Exchange Membranes, and Nylon Membranes: Humidity Influences, *Environ Sci Technol*, 49,
495 6102-6108, 10.1021/acs.est.5b00098, 2015, doi: 10.1021/acs.est.5b00098.
- 496 Huang, K., Fu, J. S., Hsu, N. C., Gao, Y., Dong, X., Tsay, S.-C., and Lam, Y. F.: Impact assessment of biomass burning
497 on air quality in Southeast and East Asia during BASE-ASIA, *Atmospheric Environment*, 78, 291-302, 2013b,
498 doi:10.1016/j.atmosenv.2012.03.048.
- 499 Jiang, G.-B., Shi, J.-B., and Feng, X.-B.: Mercury pollution in China, *Environmental science & technology*, 40, 3672-
500 3678, 2006, doi: 10.1021/es062707c.
- 501 Kang, S. C., Huang, J., Wang, F. Y., Zhang, Q. G., Zhang, Y. L., Li, C. L., Wang, L., Chen, P. F., Sharma, C. M., Li,
502 Q., Sillanpaa, M., Hou, J. Z., Xu, B. Q., and Guo, J. M.: Atmospheric Mercury Depositional Chronology Reconstructed
503 from Lake Sediments and Ice Core in the Himalayas and Tibetan Plateau, *Environ Sci Technol*, 50, 2859-2869,
504 10.1021/acs.est.5b04172, 2016, doi: 10.1021/acs.est.5b04172.



- 505 Kellerhals, M., Beauchamp, S., Belzer, W., Blanchard, P., Froude, F., Harvey, B., McDonald, K., Pilote, M., Poissant,
506 L., and Puckett, K.: Temporal and spatial variability of total gaseous mercury in Canada: results from the Canadian
507 Atmospheric Mercury Measurement Network (CAMNet), *Atmospheric Environment*, 37, 1003-1011, 2003,
508 doi:10.1016/S1352-2310(02)00917-2.
- 509 Kim, K.-H., Ebinghaus, R., Schroeder, W., Blanchard, P., Kock, H., Steffen, A., Froude, F., Kim, M.-Y., Hong, S., and
510 Kim, J.-H.: Atmospheric mercury concentrations from several observatory sites in the Northern Hemisphere, *Journal*
511 *of Atmospheric Chemistry*, 50, 1-24, 2005, doi: 10.1007/s10874-005-9222-0.
- 512 Kock, H., Bieber, E., Ebinghaus, R., Spain, T., and Thees, B.: Comparison of long-term trends and seasonal variations
513 of atmospheric mercury concentrations at the two European coastal monitoring stations Mace Head, Ireland, and
514 Zingst, Germany, *Atmospheric Environment*, 39, 7549-7556, 2005, doi:10.1016/j.atmosenv.2005.02.059.
- 515 Landis, M. S., Stevens, R. K., Schaedlich, F., and Prestbo, E. M.: Development and characterization of an annular
516 denuder methodology for the measurement of divalent inorganic reactive gaseous mercury in ambient air,
517 *Environmental science & technology*, 36, 3000-3009, 2002, doi: 10.1021/es015887t.
- 518 Lawrence, M., and Lelieveld, J.: Atmospheric pollutant outflow from southern Asia: a review, *Atmospheric Chemistry*
519 *and Physics*, 10, 11017-11096, 2010, doi:10.5194/acp-10-11017-2010.
- 520 Lee, G. S., Kim, P. R., Han, Y. J., Holsen, T. M., Seo, Y. S., and Yi, S. M.: Atmospheric speciated mercury
521 concentrations on an island between China and Korea: sources and transport pathways, *Atmos Chem Phys*, 16, 4119-
522 4133, 2016, doi:10.5194/acp-16-4119-2016.
- 523 Lelieveld, J. o., Crutzen, P., Ramanathan, V., Andreae, M., Brenninkmeijer, C., Campos, T., Cass, G., Dickerson, R.,
524 Fischer, H., and De Gouw, J.: The Indian Ocean experiment: widespread air pollution from South and Southeast Asia,
525 *Science*, 291, 1031-1036, 2001, doi: 10.1126/science.1057103.
- 526 Li, P., Feng, X., Qiu, G., Shang, L., and Li, Z.: Mercury pollution in Asia: a review of the contaminated sites, *Journal*
527 *of Hazardous Materials*, 168, 591-601, 2009, doi:10.1016/j.jhazmat.2009.03.031.
- 528 Lin, N.-H., Tsay, S.-C., Maring, H. B., Yen, M.-C., Sheu, G.-R., Wang, S.-H., Chi, K. H., Chuang, M.-T., Ou-Yang,
529 C.-F., and Fu, J. S.: An overview of regional experiments on biomass burning aerosols and related pollutants in
530 Southeast Asia: From BASE-ASIA and the Dongsha Experiment to 7-SEAS, *Atmospheric Environment*, 78, 1-19,
531 2013, doi:10.1016/j.atmosenv.2013.04.066.
- 532 Lindberg, S., Bullock, R., Ebinghaus, R., Engstrom, D., Feng, X., Fitzgerald, W., Pirrone, N., Prestbo, E., and Seigneur,
533 C.: A synthesis of progress and uncertainties in attributing the sources of mercury in deposition, *AMBIO: A Journal*
534 *of the Human Environment*, 36, 19-33, 2007, doi: 10.1579/0044-7447(2007)36[19:ASOPAU]2.0.CO;2.
- 535 Liu, W., Fox, J. E., and Xu, Z.: Litterfall and nutrient dynamics in a montane moist evergreen broad-leaved forest in
536 Ailao Mountains, SW China, *Plant Ecology*, 164, 157-170, 2003a, doi: 10.1023/A:1021201012950.
- 537 Liu, W. Y., Fox, J. E. D., and Xu, Z. F.: Nutrient budget of a montane evergreen broad-leaved forest at Ailao Mountain
538 National Nature Reserve, Yunnan, southwest China, *Hydrol Process*, 17, 1119-1134, 2003b, doi: 10.1002/hyp.1184.
- 539 Loewen, M., Kang, S., Armstrong, D., Zhang, Q., Tomy, G., and Wang, F.: Atmospheric transport of mercury to the
540 Tibetan Plateau, *Environmental science & technology*, 41, 7632-7638, 2007, doi: 10.1021/es0710398.



- 541 Loewen, M. D., Sharma, S., Tomy, G., Wang, F., Bullock, P., and Wania, F.: Persistent organic pollutants and
542 mercury in the Himalaya, *Aquatic Ecosystem Health & Management*, 8, 223-233, 2005,
543 doi:10.1080/14634980500220924.
- 544 Mukherjee, A. B., Bhattacharya, P., Sarkar, A., and Zevenhoven, R.: Mercury emissions from industrial sources in
545 India and its effects in the environment, in: *Mercury Fate and Transport in the Global Atmosphere*, Springer, 81-112,
546 2009, doi: 10.1007/978-0-387-93958-2_4.
- 547 Pacyna, E. G., Pacyna, J., Sundseth, K., Munthe, J., Kindbom, K., Wilson, S., Steenhuisen, F., and Maxson, P.: Global
548 emission of mercury to the atmosphere from anthropogenic sources in 2005 and projections to 2020, *Atmospheric*
549 *Environment*, 44, 2487-2499, 2010, doi:10.1016/j.atmosenv.2009.06.009.
- 550 Pervez, S., Koshle, A., and Pervez, Y.: Study of spatiotemporal variation of atmospheric mercury and its human
551 exposure around an integrated steel plant, India, *Atmospheric Chemistry and Physics*, 10, 5535-5549, 2010,
552 doi:10.5194/acp-10-5535-2010.
- 553 Pirrone, N., Cinnirella, S., Feng, X., Finkelman, R. B., Friedli, H. R., Leaner, J., Mason, R., Mukherjee, A. B., Stracher,
554 G., and Streets, D. G.: Global mercury emissions to the atmosphere from natural and anthropogenic sources, in:
555 *Mercury fate and transport in the global atmosphere*, Springer, 1-47, 2009, doi:10.1007/978-0-387-93958-2_1.
- 556 Pirrone, N., Cinnirella, S., Feng, X., Finkelman, R., Friedli, H., Leaner, J., Mason, R., Mukherjee, A., Stracher, G.,
557 and Streets, D.: Global mercury emissions to the atmosphere from anthropogenic and natural sources, *Atmospheric*
558 *Chemistry and Physics*, 10, 5951-5964, 2010, doi:10.5194/acp-10-5951-2010.
- 559 Rajgopal, T.: Mercury pollution in India, *The Lancet*, 362, 1856-1857, 2003, doi: 10.1016/S0140-6736(03)14936-7.
- 560 Reid, J. S., Hyer, E. J., Johnson, R. S., Holben, B. N., Yokelson, R. J., Zhang, J., Campbell, J. R., Christopher, S. A.,
561 Di Girolamo, L., and Giglio, L.: Observing and understanding the Southeast Asian aerosol system by remote sensing:
562 An initial review and analysis for the Seven Southeast Asian Studies (7SEAS) program, *Atmospheric Research*, 122,
563 403-468, 2013, doi:10.1016/j.atmosres.2012.06.005.
- 564 Schroeder, W. H., and Munthe, J.: Atmospheric mercury—an overview, *Atmospheric Environment*, 32, 809-822, 1998,
565 doi:10.1016/S1352-2310(97)00293-8.
- 566 Sheu, G.-R., Lin, N.-H., Wang, J.-L., Lee, C.-T., Ou Yang, C.-F., and Wang, S.-H.: Temporal distribution and potential
567 sources of atmospheric mercury measured at a high-elevation background station in Taiwan, *Atmospheric*
568 *Environment*, 44, 2393-2400, 2010a, doi:10.1016/j.atmosenv.2010.04.009.
- 569 Sheu, G.-R., Lin, N.-H., Lee, C.-T., Wang, J.-L., Chuang, M.-T., Wang, S.-H., Chi, K. H., and Ou-Yang, C.-F.:
570 Distribution of atmospheric mercury in northern Southeast Asia and South China Sea during Dongsha Experiment,
571 *Atmospheric Environment*, 78, 174-183, 2013, doi:10.1016/j.atmosenv.2012.07.002.
- 572 Sigler, J. M., Lee, X., and Munger, W.: Emission and long-range transport of gaseous mercury from a large-scale
573 Canadian boreal forest fire, *Environ Sci Technol*, 37, 4343-4347, 2003, doi: 10.1021/es026401r.
- 574 Slemr, F., Angot, H., Dommergue, A., Magand, O., Barret, M., Weigelt, A., Ebinghaus, R., Brunke, E. G., Pfaffhuber,
575 K. A., Edwards, G., Howard, D., Powell, J., Keywood, M., and Wang, F.: Comparison of mercury concentrations
576 measured at several sites in the Southern Hemisphere, *Atmos Chem Phys*, 15, 3125-3133, 2015, doi:10.5194/acp-15-
577 3125-2015.



- 578 Sprovieri, F., Pirrone, N., Ebinghaus, R., Kock, H., and Dommergue, A.: A review of worldwide atmospheric mercury
579 measurements, *Atmospheric Chemistry and Physics*, 10, 8245-8265, 2010, doi:10.5194/acp-10-8245-2010.
- 580 Sprovieri, F., Gratz, L., and Pirrone, N.: Development of a Ground-Based Atmospheric Monitoring Network for the
581 Global Mercury Observation System (GMOS), *E3S Web of Conferences*, 2013, 17007, doi:
582 <http://dx.doi.org/10.1051/e3sconf/20130117007>.
- 583 Swartzendruber, P. C., Jaffe, D. A., and Finley, B.: Improved fluorescence peak integration in the Tekran 2537 for
584 applications with sub-optimal sample loadings, *Atmos Environ*, 43, 3648-3651, 2009,
585 doi:10.1016/j.atmosenv.2009.02.063.
- 586 Tseng, C., Liu, C.-S., and Lamborg, C.: Seasonal changes in gaseous elemental mercury in relation to monsoon cycling
587 over the northern South China Sea, *Atmospheric Chemistry and Physics*, 12, 7341-7350, 2012, doi:10.5194/acp-12-
588 7341-2012.
- 589 Venter, A. D., Beukes, J. P., van Zyl, P. G., Brunke, E. G., Labuschagne, C., Slemr, F., Ebinghaus, R., and Kock, H.:
590 Statistical exploration of gaseous elemental mercury (GEM) measured at Cape Point from 2007 to 2011, *Atmos Chem*
591 *Phys*, 15, 10271-10280, 2015, doi:10.5194/acp-15-10271-2015.
- 592 Wang, C., Kim, D., Ekman, A. M., Barth, M. C., and Rasch, P. J.: Impact of anthropogenic aerosols on Indian summer
593 monsoon, *Geophysical Research Letters*, 36, 2009, doi: 10.1029/2009GL040114.
- 594 Wang, D., He, L., Wei, S., and Feng, X.: Estimation of mercury emission from different sources to atmosphere in
595 Chongqing, China, *Science of the total environment*, 366, 722-728, 2006, doi:10.1016/j.scitotenv.2005.09.054.
- 596 Wang, X., Zhang, H., Lin, C. J., Fu, X. W., Zhang, Y. P., and Feng, X. B.: Transboundary transport and deposition of
597 Hg emission from springtime biomass burning in the Indo-China Peninsula, *J Geophys Res-Atmos*, 120, 9758-9771,
598 2015, doi: 10.1002/2015JD023525.
- 599 Wooster, M. J., Roberts, G., Perry, G. L. W., and Kaufman, Y. J.: Retrieval of biomass combustion rates and totals
600 from fire radiative power observations: FRP derivation and calibration relationships between biomass consumption
601 and fire radiative energy release, *J Geophys Res-Atmos*, 110, 2005, doi: 10.1029/2005JD006318.
- 602 Wu, Y., Wang, S., Streets, D. G., Hao, J., Chan, M., and Jiang, J.: Trends in anthropogenic mercury emissions in China
603 from 1995 to 2003, *Environmental Science & Technology*, 40, 5312-5318, 2006, doi: 10.1021/es060406x.
- 604 Xiao, Z., Sommar, J., Wei, S., and Lindqvist, O.: Sampling and determination of gas phase divalent mercury in the air
605 using a KCl coated denuder, *Fresenius' journal of analytical chemistry*, 358, 386-391, 1997, doi:
606 10.1007/s002160050434.
- 607 Xu, B., Cao, J., Hansen, J., Yao, T., Joswia, D. R., Wang, N., Wu, G., Wang, M., Zhao, H., and Yang, W.: Black soot
608 and the survival of Tibetan glaciers, *Proceedings of the National Academy of Sciences*, 106, 22114-22118, 2009,
609 doi: 10.1073/pnas.0910444106.
- 610 Yao, T., Thompson, L., Yang, W., Yu, W., Gao, Y., Guo, X., Yang, X., Duan, K., Zhao, H., and Xu, B.: Different glacier
611 status with atmospheric circulations in Tibetan Plateau and surroundings, *Nature Climate Change*, 2, 663-667, 2012,
612 doi:10.1038/nclimate1580.
- 613 You, G., Zhang, Y., Liu, Y., Schaefer, D., Gong, H., Gao, J., Lu, Z., Song, Q., Zhao, J., and Wu, C.: Investigation of
614 temperature and aridity at different elevations of Mt. Ailao, SW China, *International journal of biometeorology*, 1-6,



615 2012, doi: 10.1007/s00484-012-0570-6.

616 Yu, B., Wang, X., Lin, C. J., Fu, X. W., Zhang, H., Shang, L. H., and Feng, X. B.: Characteristics and potential sources
617 of atmospheric mercury at a subtropical near-coastal site in East China, *J Geophys Res-Atmos*, 120, 8563-8574,
618 10.1002/2015JD023425, 2015, doi: 10.1002/2015JD023425.

619 Yuhong, Z. K. M. Y. L., and Yourong, L.: Agriculture significance of the foehn effect in the SW monsoon: A case study
620 in the Ailao mountain, *Journal of Mountain Research*, 2, 002, 1993.

621 Zhang, G., Li, J., Li, X.-D., Xu, Y., Guo, L.-L., Tang, J.-H., Lee, C. S., Liu, X., and Chen, Y.-J.: Impact of
622 anthropogenic emissions and open biomass burning on regional carbonaceous aerosols in South China, *Environmental*
623 *Pollution*, 158, 3392-3400, 2010, doi:10.1016/j.envpol.2010.07.036.

624 Zhang, H., Yin, R.-s., Feng, X.-b., Sommar, J., Anderson, C. W., Sapkota, A., Fu, X.-w., and Larssen, T.:
625 Atmospheric mercury inputs in montane soils increase with elevation: evidence from mercury isotope signatures,
626 *Scientific reports*, 3, 2013, doi: 10.1038/srep03322.

627 Zhang, H., Fu, X. W., Lin, C. J., Wang, X., and Feng, X. B.: Observation and analysis of speciated atmospheric
628 mercury in Shangri-La, Tibetan Plateau, China, *Atmos Chem Phys*, 15, 653-665, 2015, doi:10.5194/acp-15-653-2015.

629 Zhang, Q. G., Huang, J., Wang, F. Y., Mark, L. W., Xu, J. Z., Armstrong, D., Li, C. L., Zhang, Y. L., and Kang, S. C.:
630 Mercury Distribution and Deposition in Glacier Snow over Western China, *Environ Sci Technol*, 46, 5404-5413, 2012,
631 doi: 10.1021/es300166x.

632 ZHAO, D., YAO, P., YANG, R.-w., and CAO, J.: The spatial and temporal distribution features of onset period of
633 mean rainy season over Asian monsoon region, *Journal of Yunnan University (Natural Sciences Edition)*, 4, 012, 2006.

634

635

636

637

638

639

640

641

642

643

644

645

646

647

648

649

650



651

652 **Figure Captions**

653

654 **Table 1:** The statistics for mercury species and meteorological variables based on daily averages from May
655 2010 through May 2011 at the ALS site.

656 **Fig. 1:** Map showing the location of ALS, anthropogenic mercury emissions ($\text{g km}^{-2} \text{y}^{-1}$) and major cities in Asia
657 (AMAP/UNEP, 2013).

658 **Fig. 2:** Total gaseous mercury (TGM) concentration in the ambient air at ALS. Source 1 represents the peaks of
659 high TGM concentrations at ALS during the ISM period, which were caused by anthropogenic Hg emissions
660 from inland China due to the strengthening of EASM. Source 2 represents the peaks of high TGM concentrations
661 at ALS during the non-ISM period, which were caused by the biomass burning from Southeast Asia and
662 anthropogenic Hg emissions from South Asia.

663 **Fig. 3:** Monthly TGM anomalies at ALS. The Hg concentration during the ISM period (May to September) was
664 higher than that of the non-ISM period (October to April). The highest monthly concentration (2.46 ng m^{-3}) was
665 observed in May, and the lowest monthly mean concentration (1.45 ng m^{-3}) was observed in November. The air
666 temperature was higher, and the wind speed was lower during the ISM period than that of the non-ISM period.

667 **Fig. 4:** Distribution frequency of TGM above and under the average (2.09 ng m^{-3}) based on wind direction
668 during the ISM and the non-ISM period. The high and low Hg levels of the SW frequency was higher than
669 both the high and low Hg levels of the NE and SE frequencies.

670 **Fig. 5:** TGM, GOM and PBM variation during the ISM and non-ISM period based on the four sampling
671 campaigns. TGM, GOM and PBM concentrations showed a monsoonal variation with higher level during the
672 ISM period than in the non-ISM period.

673 **Fig. 6:** Pollution roses of Hg species. Most of the TGM, GOM and PBM were from SW, and some higher TGM,
674 GOM and PBM events were from NE during the ISM period. Almost all TGM, GOM and PBM were from SW
675 during the non-ISM period.

676 **Fig. 7:** Air mass backward trajectory analysis for long range transport to ALS. Most of these backward
677 trajectories consisted of air masses that originated from South and Southeast Asia and were accompanied by
678 lower Hg levels. Air masses originating from inland China were less frequent and accompanied by higher Hg
679 levels.

680 **Fig. 8:** The distribution of the Indian monsoon index (IMI), TGM and rainfall at ALS. IMI displays that the ISM
681 period was from May to September. RF events mainly appeared during the ISM period. Some high Hg events
682 were accompanied by NE and east wind events during the ISM period. High TGM events were accompanied by
683 the appearance of SW during the non-ISM period.

684 **Fig. 9:** Backward trajectories of air masses and the variation of TGM concentrations because of the strengthening
685 of and incursion of air flow from EASM on June 23-28, 2011 (a), and July 10-18, 2011 (b), during the ISM
686 period (May to September). The TGM level (C) were 3.27 ng m^{-3} (a) and 3.65 ng m^{-3} (b) with the air masses from



687 important industrial regions of inland China. The TGM level were down to 2.49 ng m⁻³(a) and 3.02 ng m⁻³(b)
688 while the air flow shifted to southwest and swept Southeast Asia.

689 **Fig. 10:** Backward trajectories of air masses and the variation of TGM concentrations because of the
690 strengthening and incursion of air flow from EASM and the cold Siberian current from September 28 to October
691 9, 2011, during the non-ISM period (October to April). The TGM level (C) were 2.25 ng m⁻³, 3.18 ng m⁻³ and
692 2.53 ng m⁻³ with the air masses from inland China. The TGM level was down to 1.89 ng m⁻³ with the air masses
693 from South China Sea, northern Vietnam and Laos.

694 **Fig. 11:** Backward trajectories of air masses and the sites of fire events from December 23-31, 2011, during the
695 non-ISM period (October to April). The TGM level (C) was 3.13 ng m⁻³ with air masses from important
696 Southeast Asia industrial regions. The TGM level dropped to 2.78 ng m⁻³ with air masses from the Bay of Bengal.

697 **Fig. 12:** Correlation of TGM and CO in December 23-31, 2011, during the non-ISM period.

698 **Fig. 13:** Backward trajectories of air masses and the sites of fire events in March 23-29, 2012, during the non-
699 ISM period (October to April). The TGM level (C) were 4.53 ng m⁻³ with the air masses from inland China. The
700 TGM level was 3.11 ng m⁻³ with the air masses from Myanmar and high-frequency fire events.

701 **Fig. 14:** Correlation of TGM and CO ($R^2=0.53$), correlations between TFRP (total fire radiative power) and CO
702 ($R^2=0.98$) and TGM ($R^2=0.45$) in March 23-29, 2012, during the non-ISM period (October to April).

703 **Fig. 15:** Potential source regions and pathways of atmospheric TGM at ALS as identified by the CWT during
704 the ISM period (a, May to September) and the non-ISM period (b, October to April).

705



706 **Table 1:** The statistics for mercury species and meteorological variables based on daily averages from May

707 2010 through May 2011 at the ALS site.

708

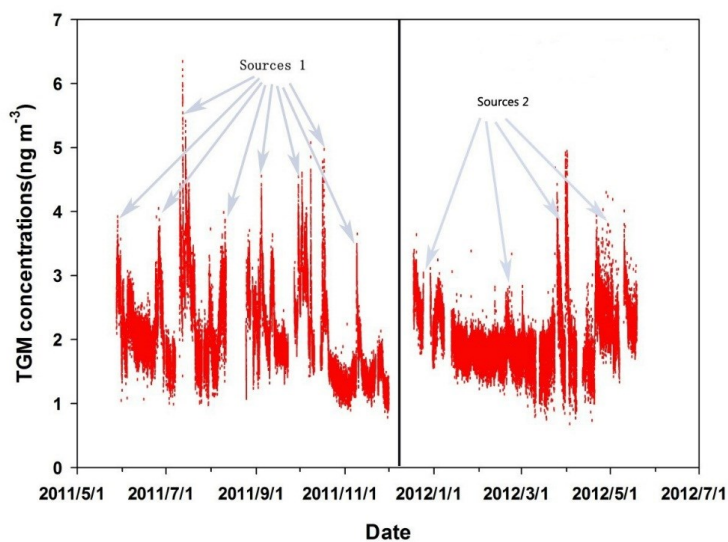
		Spring	Summer	Autumn	Winter	ISM period	Non-ISM period	Total
TGM (ng m ⁻³)	Mean	2.18	2.20	1.92	2.04	2.22	1.99	2.09
	±SD	0.67	0.60	0.64	0.58	0.58	0.66	0.63
	Range	1.01-5.70	1.15-3.79	1.11-3.59	0.99-4.45	1.01-3.79	0.99-5.70	0.99-5.70
GOM (pg m ⁻³)	Mean	2.31	2.04	3.42	1.83	2.45	2.06	2.22
	±St.Dev	1.79	1.39	2.99	2.85	2.08	2.40	2.28
	Range	0.13-10.20	0.27-6.68	0.11-13.29	0.12-17.25	0.11-13.29	0.12-17.25	0.11-17.25
PBM (pg m ⁻³)	Mean	22.39	32.19	46.28	31.97	36.38	27.36	31.27
	±St.Dev	19.05	30.56	28.80	30.63	30.62	26.09	28.44
	Range	0.87-135.79	5.84-165.01	16.16-120.99	3.84-139.65	5.84-165.01	0.87-139.65	0.87-165.01
AT (°C)	Mean	13.36	15.53	11.42	6.96	15.45	8.93	11.95
	±St.Dev	3.03	1.19	3.39	1.88	1.29	2.93	3.99
	Range	4.88-18.38	11.66-17.74	4.78-16.18	1.65-10.83	11.32-18.38	1.65-15.16	1.65-18.38
RH (%)	Mean	72.26	90.77	91.11	73.58	87.43	75.77	81.17
	±St.Dev	15.06	5.56	4.94	18.17	9.58	17.48	15.49
	Range	38.42-97.63	71.17-99.25	79.96-100.00	33.17-100.00	52.25-99.25	33.17-100.00	33.17-100.00
WS (m/s)	Mean	3.60	2.59	2.71	4.29	2.59	3.80	3.29
	±St.Dev	0.42	0.47	0.38	0.07	0.45	0.55	0.79
	Range	2.99-3.95	2.05-3.19	2.17-2.97	4.20-4.37	2.05-3.19	2.97-4.37	2.05-4.37
RF (mm)	Total	334.3	845.4	612.4	44.2	1493	343.3	1836.3
WD (%)	NE	3.25	15.22	14.03	0	11.35	5.46	7.79
	SE	9.76	14.13	20.65	4.0	16.22	10.33	13.07
	SW	86.99	66.30	64.13	95.60	71.89	84.98	78.89
	NW	0	0	0	0	0	0	0

709

710



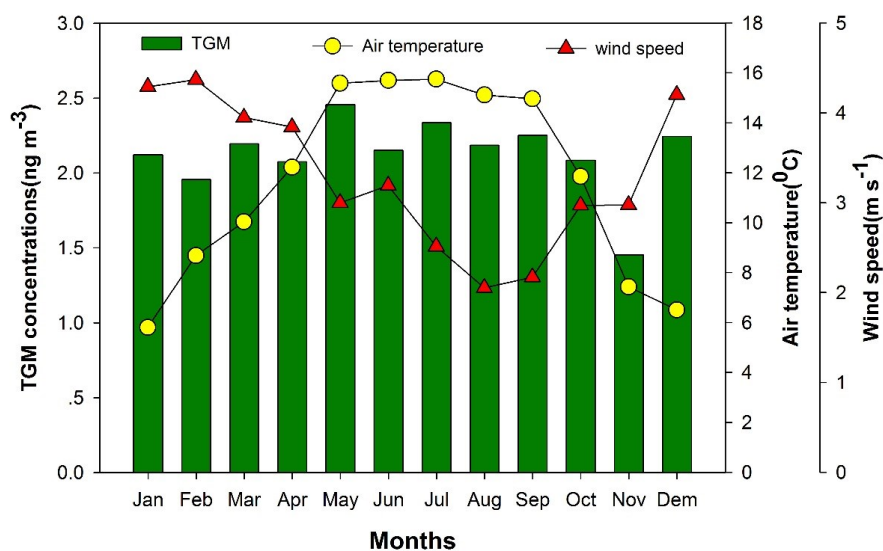
716 **Fig. 2:** Total gaseous mercury (TGM) concentration in the ambient air at ALS. Source 1 represents the peaks of
717 high TGM concentrations at ALS during the ISM period (May to September), which were caused by
718 anthropogenic Hg emissions from inland China due to the strengthening of EASM. Source 2 represents the peaks
719 of high TGM concentrations at ALS during the non-ISM period (October to April), which were caused by the
720 biomass burning from Southeast Asia and anthropogenic Hg emissions from South Asia.
721



722
723



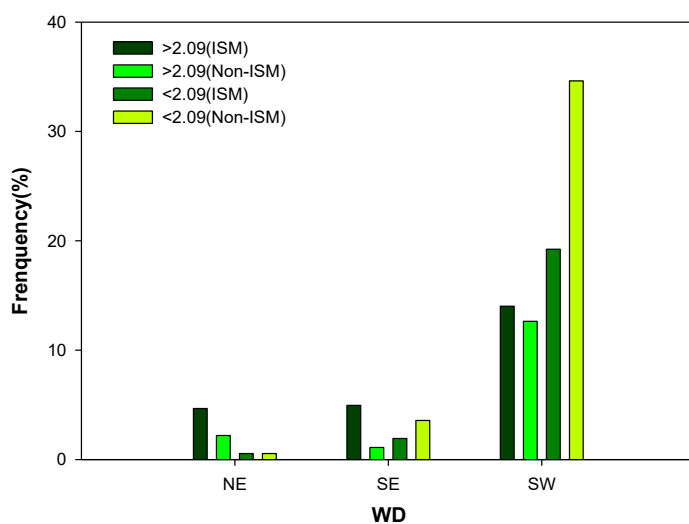
724 **Fig. 3:** Monthly TGM anomalies at ALS. The Hg concentration during the ISM period (May to September) was
725 higher than that of the non-ISM period (October to April). The highest monthly concentration (2.46 ng m^{-3}) was
726 observed in May, and the lowest monthly mean concentration (1.45 ng m^{-3}) was observed in November. The air
727 temperature was higher, and the wind speed was lower during the ISM period than that of the non-ISM period.
728



729
730



731 **Fig. 4:** Distribution frequency of TGM above and under the average (2.09 ng m^{-3}) based on wind direction
732 during the ISM (May to September) and the non-ISM period (October to April). The high and low Hg levels of
733 the SW frequency was higher than both the high and low Hg levels of the NE and SE frequencies.
734

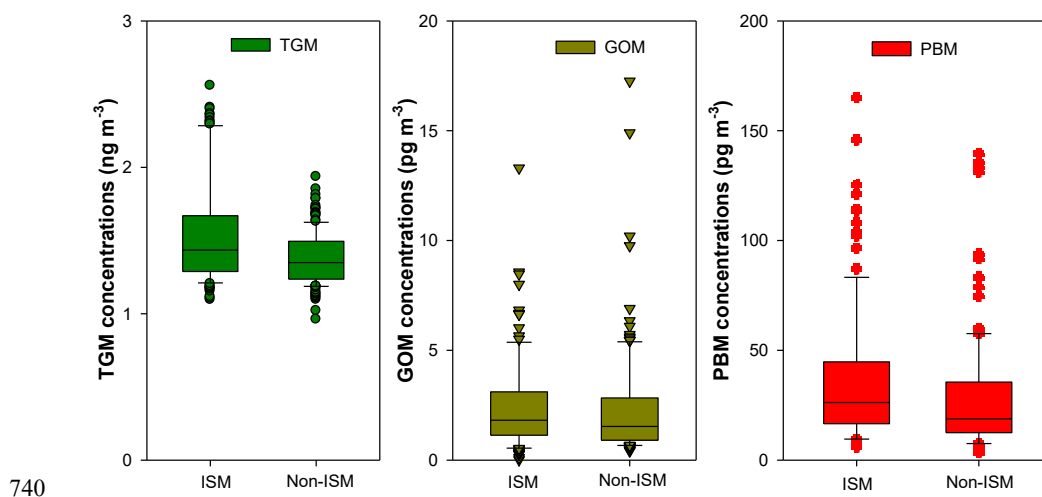


735

736

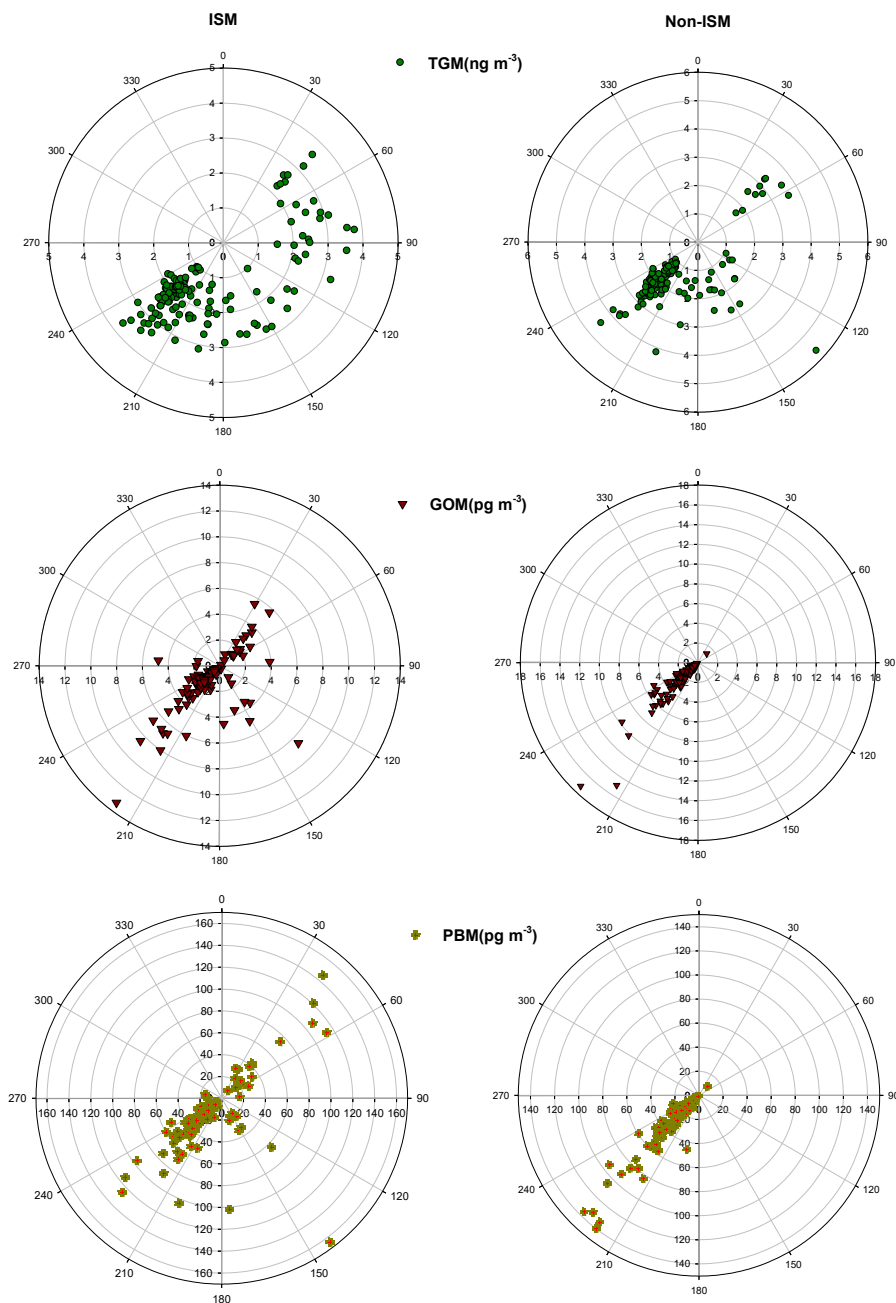


737 **Fig. 5:** TGM, GOM and PBM variation during the ISM (May to September) and non-ISM period (October to
738 April) based on the four sampling campaigns. TGM, GOM and PBM concentrations showed a monsoonal
739 variation with higher level during the ISM period than in the non-ISM period.





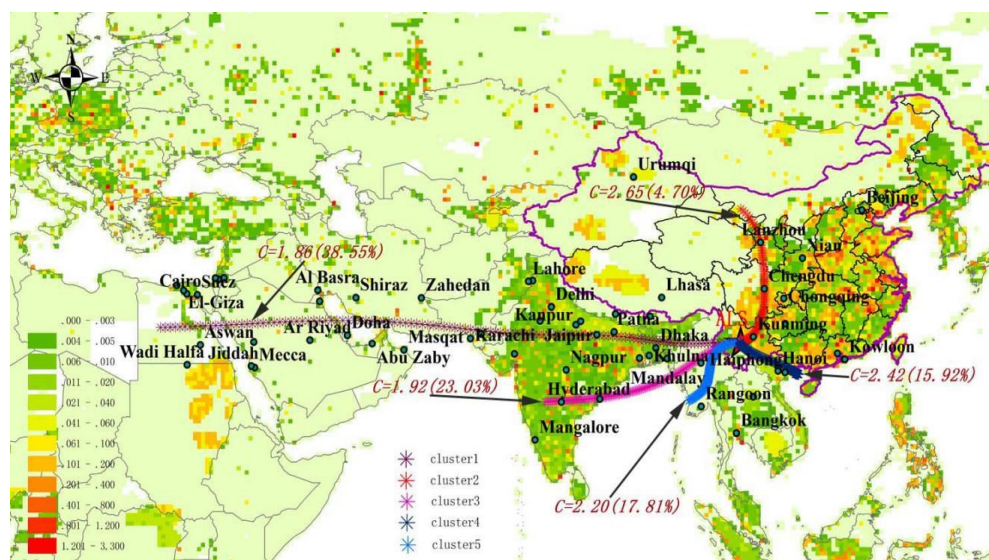
741 **Fig. 6:** Pollution roses of Hg species. Most of the TGM, GOM and PBM were from SW, and some higher TGM,
742 GOM and PBM events were from NE during the ISM period (May to September). Almost all TGM, GOM and
743 PBM were from SW during the non-ISM period (October to April).
744



745



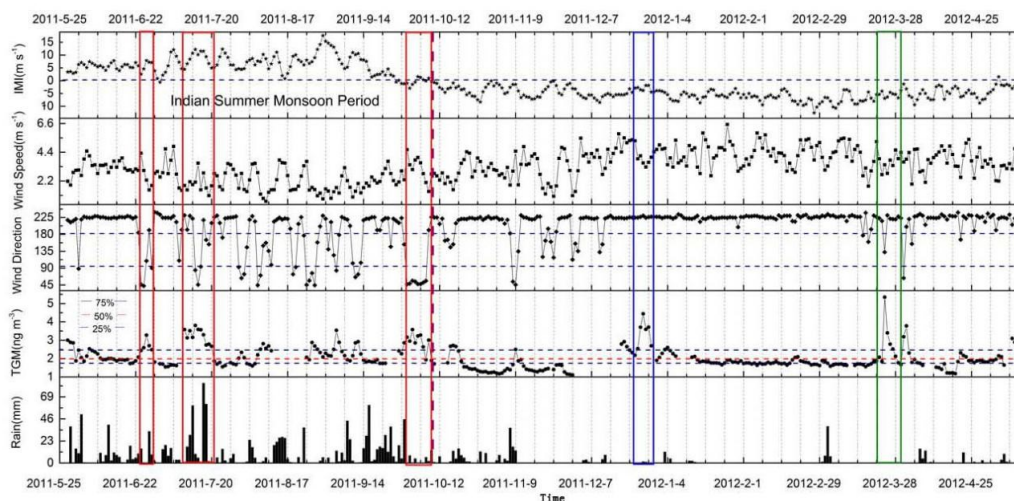
746 **Fig. 7:** Air mass backward trajectory analysis for long range transport to ALS. Most of these backward
747 trajectories consisted of air masses that originated from South and Southeast Asia and were accompanied by
748 lower Hg levels. Air masses originating from inland China were less frequent and accompanied by higher Hg
749 levels.
750



751
752



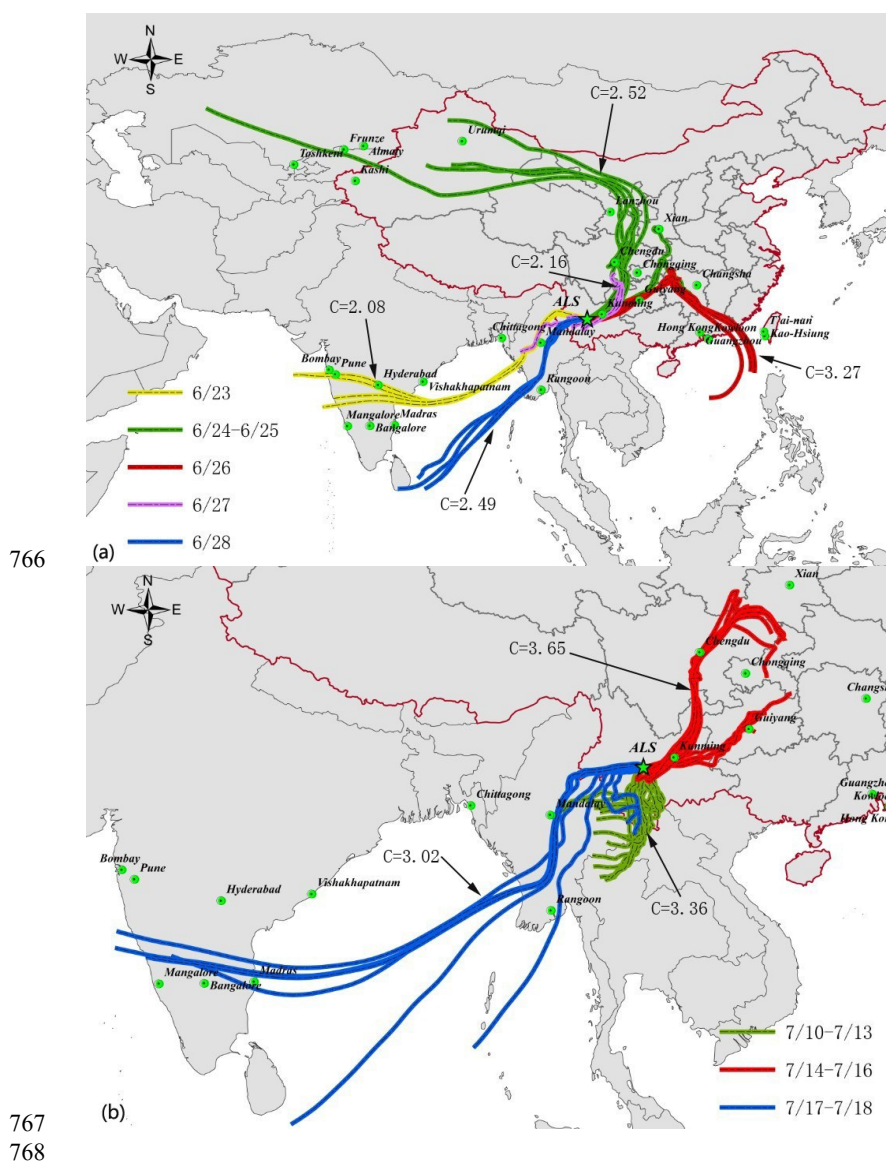
753 **Fig. 8:** The distribution of the Indian monsoon index (IMI), TGM and rainfall at ALS. IMI displays that the ISM
 754 period was from May to September. RF events mainly appeared during the ISM period. Some high Hg events
 755 were accompanied by NE and east wind events during the ISM period. High TGM events were accompanied by
 756 the appearance of SW during the non-ISM period (October to April).
 757



758
759

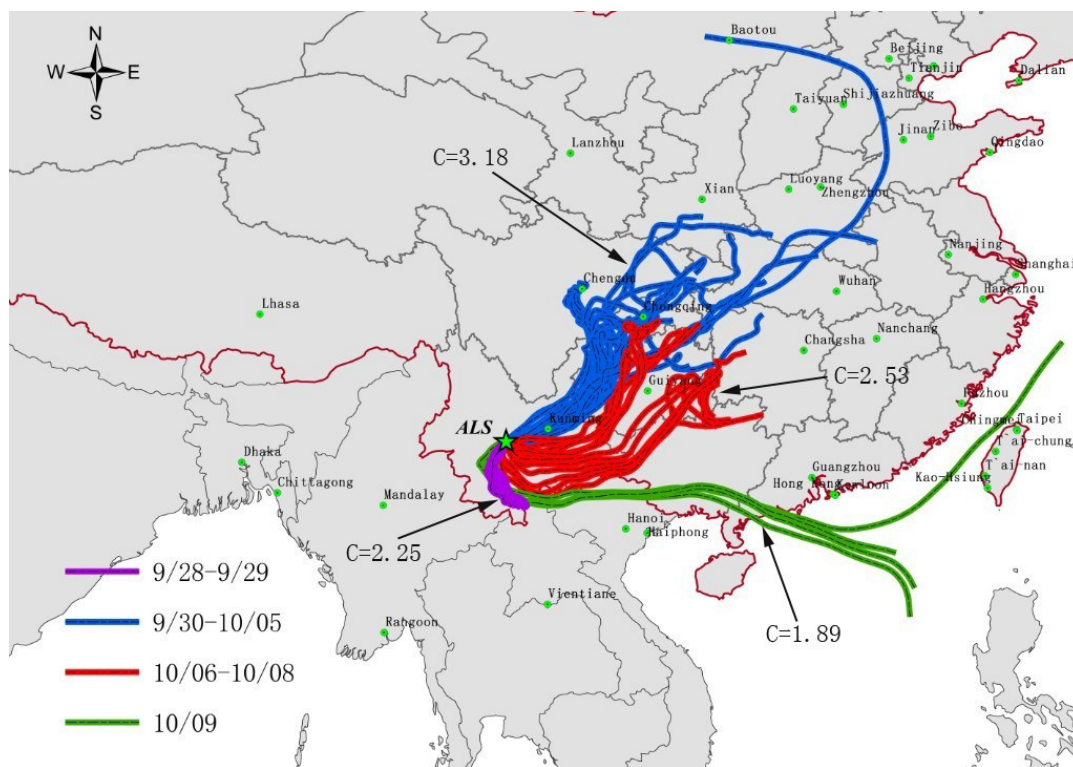


760 **Fig. 9:** Backward trajectories of air masses and the variation of TGM concentrations because of the strengthening
761 of and incursion of air flow from EASM on June 23-28, 2011 (a), and July 10-18, 2011 (b), during the ISM
762 period (May to September). The TGM level (C) were 3.27 ng m^{-3} (a) and 3.65 ng m^{-3} (b) with the air masses from
763 important industrial regions of inland China. The TGM level were down to 2.49 ng m^{-3} (a) and 3.02 ng m^{-3} (b)
764 while the air flow shifted to southwest and swept Southeast Asia.
765





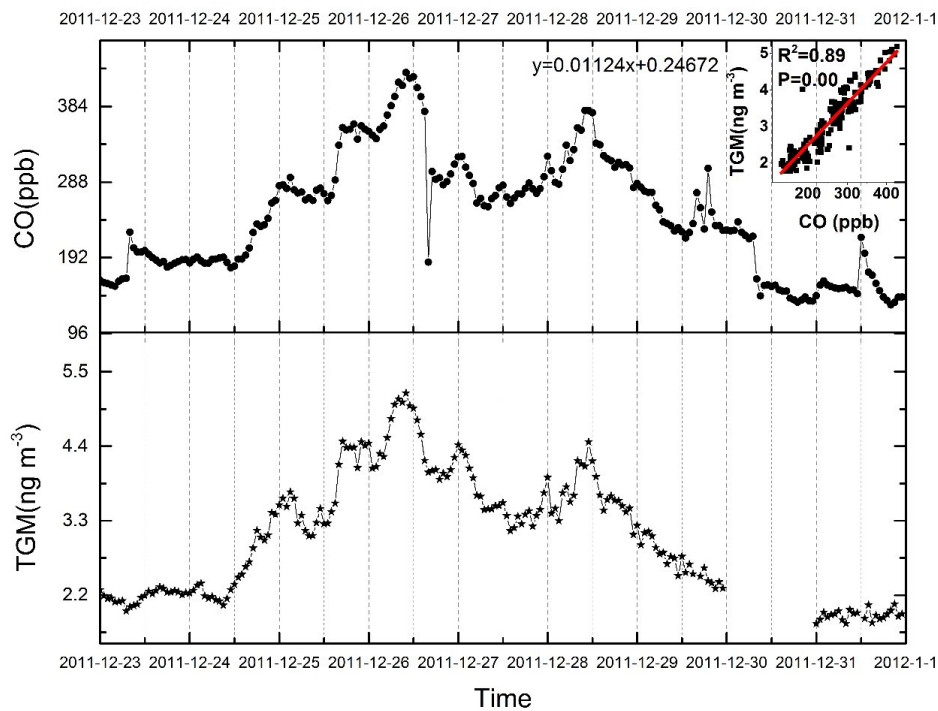
769 **Fig. 10:** Backward trajectories of air masses and the variation of TGM concentrations because of the
770 strengthening and incursion of air flow from EASM and the cold Siberian current from September 28 to October
771 9, 2011, during the non-ISM period (October to April). The TGM level (C) were 2.25 ng m⁻³, 3.18 ng m⁻³ and
772 2.53 ng m⁻³ with the air masses from inland China. The TGM level was down to 1.89 ng m⁻³ with the air masses
773 from South China Sea, northern Vietnam and Laos.
774



775
776



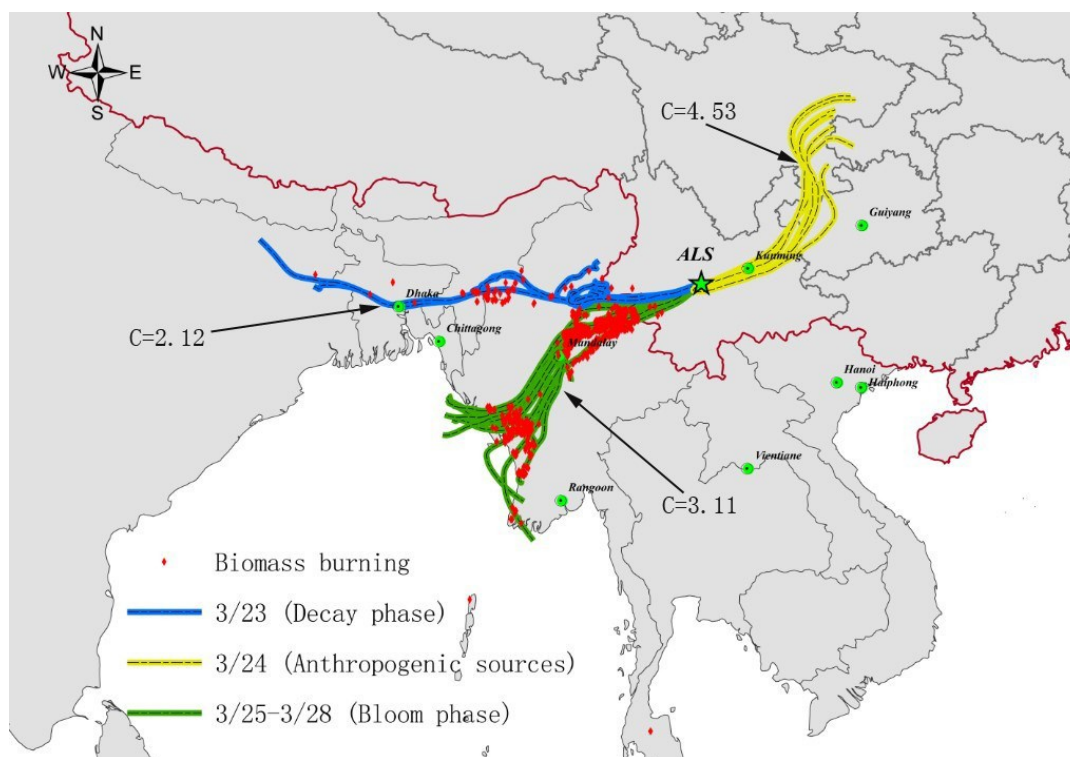
784 **Fig. 12:** Correlation of TGM and CO in December 23-31, 2011, during the non-ISM period (October to April).
785



786
787

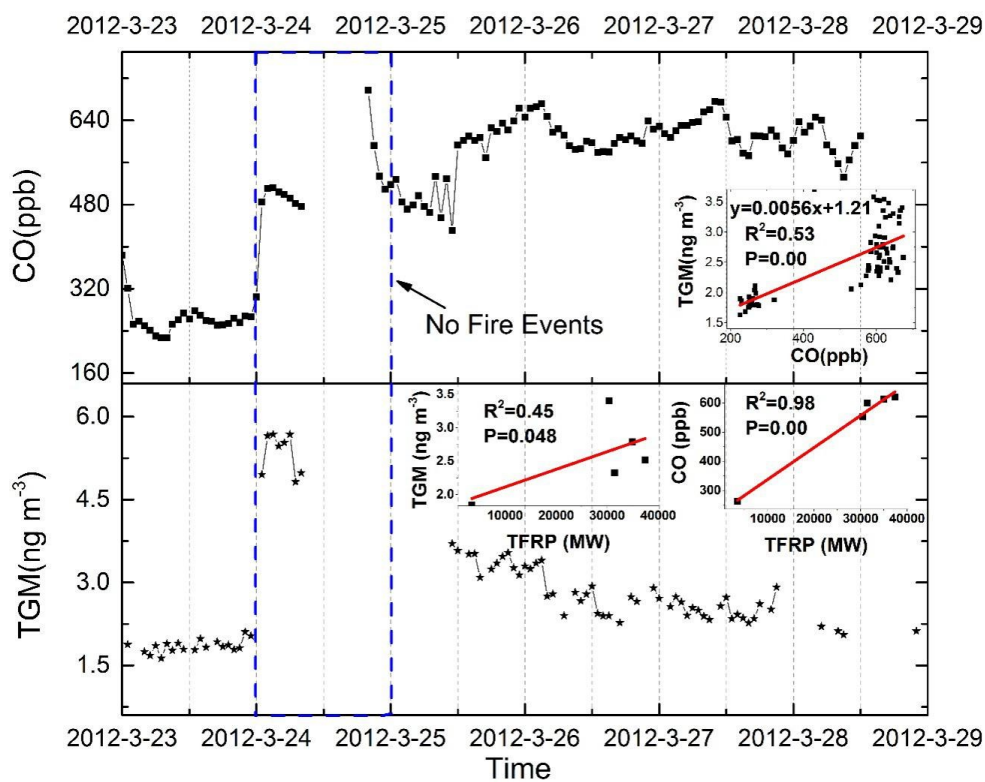


788 **Fig. 13:** Backward trajectories of air masses and the sites of fire events in March 23-29, 2012, during the non-
789 ISM period (October to April). The TGM level (C) were 4.53 ng m⁻³ with the air masses from inland China. The
790 TGM level was 3.11 ng m⁻³ with the air masses from Myanmar and high-frequency fire events.
791





794 **Fig. 14:** Correlation of TGM and CO ($R^2=0.53$), correlations between TFRP (total fire radiative power) and CO
795 ($R^2=0.98$) and TGM ($R^2=0.45$) in March 23-29, 2012, during the non-ISM period (October to April).
796

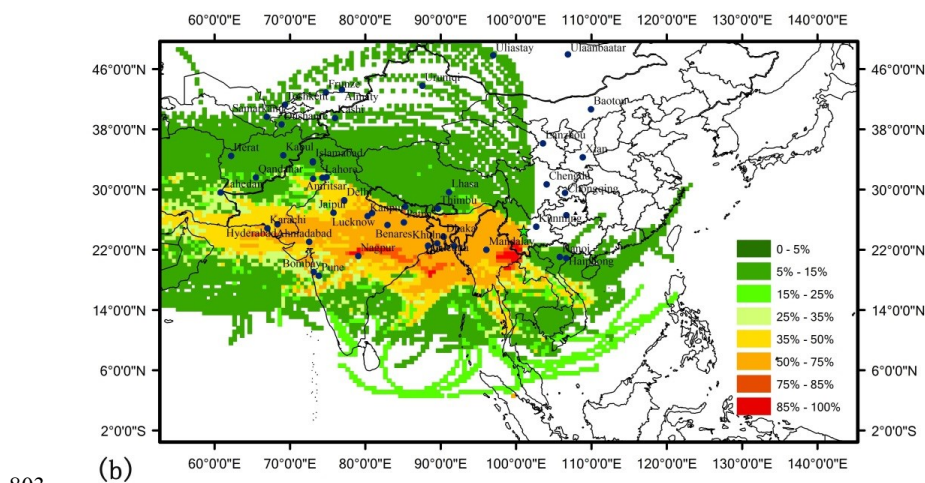
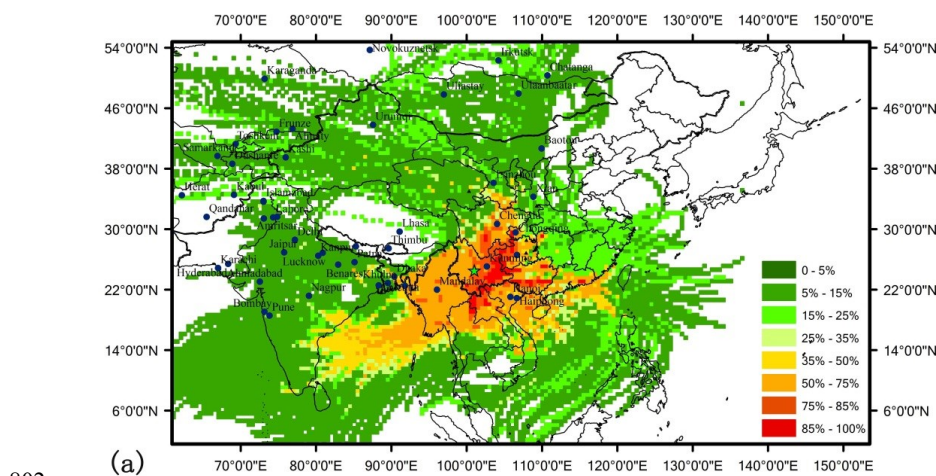


797

798



799 **Fig. 15:** Potential source regions and pathways of atmospheric TGM at ALS as identified by the CWT during
800 the ISM period (a, May to September) and the non-ISM period (b, October to April).
801



804